

Chapter 6

Computational Test Problems

Computational Fluid Dynamics is still in its infancy and at times mathematical rigour is replaced by either physical argument or empiricism. Consequently, few practical algorithms are beyond reproach. However, to employ a hackneyed phrase, the proof of the pudding is in the eating. So, we have used the AMR algorithm to compute solutions to three problems which are of genuine interest to fluid dynamicists. For each problem, we state briefly why it is of interest, present our numerical results and then compare these results qualitatively and quantitatively with experiment. Unfortunately, because traditional experimental methods provide quantitative information for only a limited number of points in the flowfield, the quantitative comparisons are not as comprehensive as we would like. Nevertheless, these test problems should still demonstrate the worth of the AMR algorithm.

6.1 Open Cylindrical Shock Tube

The time dependent behaviour of blast flowfields has been studied extensively, both computationally and experimentally. The results from such experiments and simulations are important in many practical situations. For example, they are used to determine the blast loading on structures and personnel when weapons are fired, and to find the external overpressure on a launch vehicle when its solid fuel rocket motors are ignited. From our point of view, this type of problem provides an ideal test for the AMR algorithm because the flowfield is highly unsteady and it contains many complex features which would remain under-resolved if an adaptive mesh strategy were not used. Typical of such under-resolved calculations are those presented by Wang & Widhopf[71] which were computed using a fixed zonal grid. To demonstrate the increase in resolution made possible by the AMR algorithm we tackle the same problem; a plane shock, $M_s = 1.76$ and $\gamma = 1.4$, moves from left to right down an open cylindrical shock tube, the flow being both inviscid

and axisymmetric. We validate our numerical results using the experimental results of Schmidt & Duffy[60].

6.1.1 Calculation Details

Because the flow is axisymmetric we need compute a solution for just one half of a planar slice which contains the tube's axis. Plots are presented where density contours¹ are shown for the top half of this slice, while the corresponding computational grid is shown reflected about the tube's axis. Three grid levels were used for the calculation, see figure 6.2. The grid at level 0 was 75 cells wide by 40 cells high, and the spatial refinement factors, rI and rJ , for grid levels 1 and 2 were set to 4. Thus the grid at level 2 has the same resolution as a uniform mesh of 1200 by 640 cells.

Although the flow is both inviscid and axisymmetric we do not integrate the axisymmetric Euler equations directly. Instead we compute axisymmetric solutions to the Euler equations, a natural ruse[68, 48] for finite-volume schemes. Conceptually, the computational grid is thought of as being hinged along the tube's axis, and the finite-volume mesh cells are generated by sweeping the grid through some small angle $\delta\theta$. Thus each mesh cell forms a wedge. Axisymmetric solutions may then be enforced by applying *pressure fluxes* to the side faces of each cell. This approach has two advantages. First, there is no singularity along the axis of the tube, cell areas simply shrink to zero. Second, some authors suggest that Riemann based methods should be modified to account for source terms[53, 26], but, because this approach has no source terms we can calculate interface fluxes in exactly the same way as for two-dimensional flows. Here we have used Roe's flux difference splitting scheme combined with the SUPERBEE flux limiter, see chapter 5.

The Euler equations contain no length scale and therefore the form of the solution to this open shock tube problem depends only on the initial shock Mach number, M_s , and the ratio of the specific heats for the fluid, γ . To start the calculation we have used the exact shock jump conditions. The density and pressure for the quiescent fluid were taken as unity and the flow conditions behind the shock were calculated using the moving shock relationships given in appendix A. Before our numerical results are compared to experiment they are scaled to suit the appropriate tube diameter and the temperature and pressure for the quiescent fluid. For the experiment of Schmidt & Duff[60] these scaling parameters are 15.2 cm, 295 K and 1 atm respectively.

6.1.2 Computational Results

Initially, the shock simply travels down the tube, but when it reaches the exit plane it diffracts around the lip, see figure 6.3. The pressure gradient at the lip causes the corner

¹These are drawn at 2.5% intervals.

slip line to roll up into a vortex. This flow pattern remains nearly self-similar in time until the corner expansion waves reach the axis of the tube. Note how the grid has adapted to the flow solution. The medium grid has grown to cover the full extent of the flow activity, while the fine grid covers only the diffracted shock and the lip vortex. At this stage in the calculation the AMR algorithm is very economical in terms of the number of cells it requires to resolve the flow: the medium grid is formed from 2 meshes and contains 1504 cells; the fine grid is formed from 14 meshes and contains 6080 cells. So, less than 1% of the computational domain is covered by the fine grid.

The diffracted shock eventually detaches from the tube and becomes an almost spherical blast wave, see figure 6.4. Behind this blast wave a jet like flow has evolved. A shear layer emanates from the exit lip of the tube and a shock has formed near the vortex to recompress the over expanded jet flow. This shock strengthens towards the tube's axis and forms a Mach disk. The flow at the exit of the tube is subsonic and so a rarefaction wave propagates back up the tube. The evolution of the computational grid has clearly kept pace with the evolution of this jet flow. The medium grid is now made up from 14 meshes and contains 5,136 cells, while the fine grid is formed from 64 meshes and contains 17,280 cells. The fine grid covers just over 2% of the computational domain.

As the flow continues to evolve so the strength of the jet shock increases, and both the vortex and the Mach disk move downstream, see figure 6.5. The further the Mach disk moves downstream the smaller it gets and it starts to lag behind the vortex. Re-compression shocks are clearly visible within this high speed vortex. A triple point has formed marking the intersection of the Mach disk, the jet shock and an oblique downstream shock. The slip line emanating from this triple point exhibits the early stages of a Kelvin-Helmholtz instability. The computational grid has continued to evolve with the flow. The medium grid is now formed from 22 meshes and contains 8,128 cells. While, the fine grid, which has become increasingly fragmented in the vicinity of the vortex, is formed from 98 meshes and contains a total of 21,664 cells. The Mach disk eventually reaches a stable position some 1.4 tube diameter lengths downstream of the exit plane, see figure 6.6, but the vortex continues to move downstream. The Kelvin-Helmholtz instability has become quite pronounced.

6.1.3 Comparison with Experiment

Because viscous effects are predominantly limited to the jet shear layer and the vortex core, our numerical results show excellent qualitative agreement with experiment. Compare the density contours shown in figures 6.3 and 6.6 with the shadowgraphs shown in figures 6.7 and 6.8, but note that these shadowgraphs must be correctly interpreted before any comparison is made. First, the flowfield is axisymmetric and therefore a camera will record features that would not be present if a planar slice were taken through the flowfield. For example, the projection on the film of the locus formed by a set of axisymmetric points

will appear as a line. Such lines have been marked with the label *Al*. Second, the camera was not exactly perpendicular to the jet axis and therefore the shock patterns appear as ovals instead of lines. Third, much of the flowfield appears to be turbulent simply because the camera has to look through the turbulent shear layer which emanates from the exit lip of the tube. The turbulent flow regions are in fact limited to thin axisymmetric sheets.

The resolution of our numerical results is comparable to that of the shadowgraphs. This numerical resolution is particularly impressive considering that the entire calculation took just over 12 hours processing time on a small desktop workstation² whose power rating is only 1.4 Mflops. Whilst there can be little doubt that the calculation is qualitatively correct, we can only make a limited number of quantitative comparisons. One, Schmidt & Duffy claim that the position of the Mach disk stabilises 1.34 tube diameter lengths downstream of the exit plane. For our calculation this distance is just under 1.4 tube diameter lengths, a discrepancy of about 4%. Two, the sets of angles between the shocks at the triple point, one measured from figure 6.6 the other measured from figure 6.8, agree to within $\pm 1.5^\circ$. This discrepancy is comparable to the uncertainty in their measurement. Three, figure 6.1 shows a comparison between the computational and experimental pressure history for a point located on the tube's axis, 1.5 diameter lengths downstream of the exit plane. Note, time is measured from when the shock reaches the exit plane. Up to $t = 1ms$ the numerical results closely resemble the experimental ones, in particular, the peak over-pressures agree to within 1%. Thereafter the results do not correlate. However, for $t > 1ms$ the experimental results are suspect. The position of the Mach disk stabilises approximately 1.34 diameter lengths downstream of the exit plane, so a secondary peak in the pressure history for a point 1.5 diameter lengths downstream of the exit plane is unexpected. It would appear that the pressure measuring device has influenced the flow. Note, shortly after $t = 1ms$ the vortex overtakes the Mach disk and therefore the oblique shock stretching from the triple point to the vortex core passes the position of the probe. Since the support for the measuring probe runs perpendicular to the tube's axis it will eventually interact with this shock giving rise to spurious pressure measurements.

²A Sun SPARCstation 1.

Figure 6.1: Pressure history for a point on the tube's axis, 1.5 diameter lengths downstream of the exit plane.

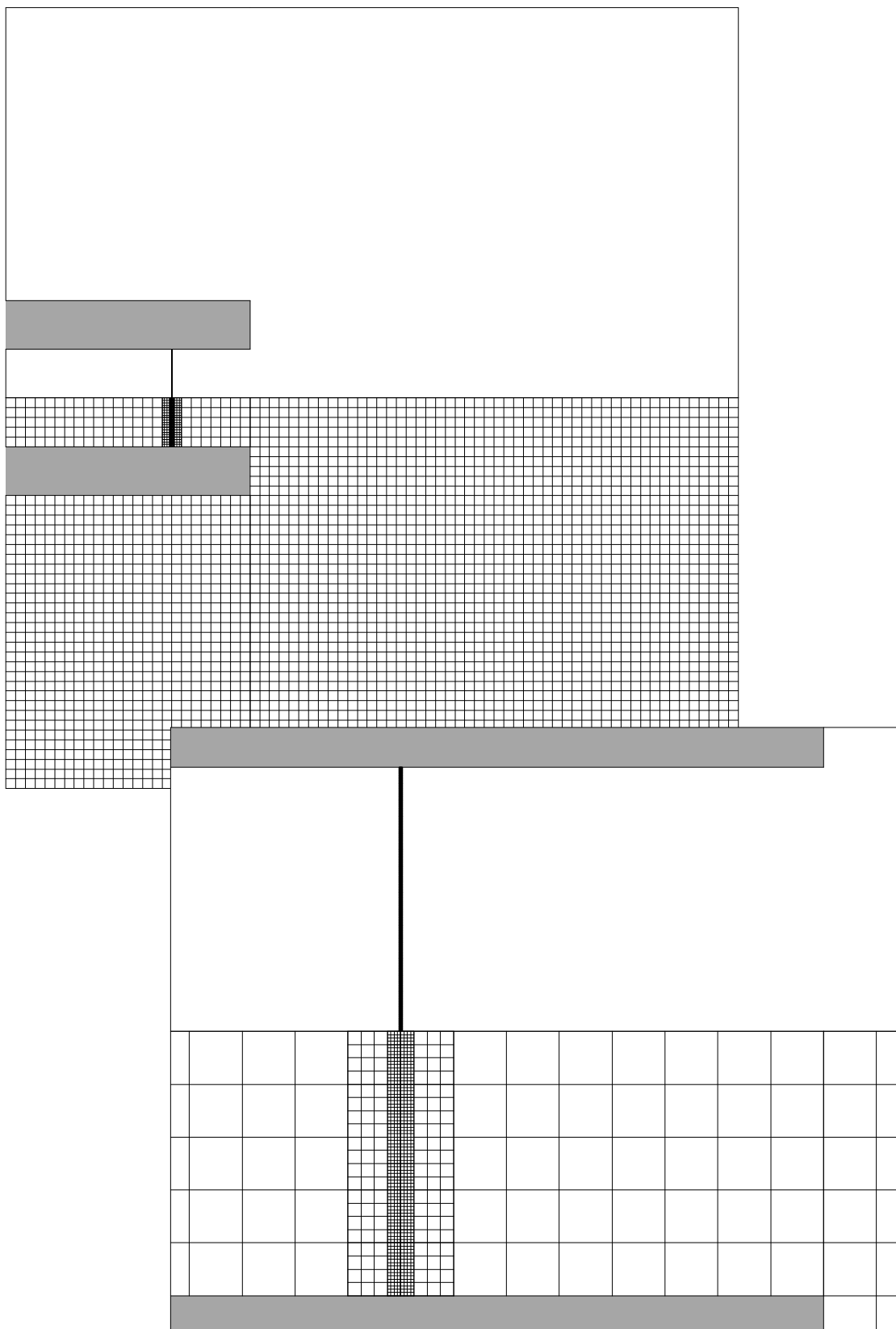


Figure 6.2: Initial conditions for the open shock tube problem.

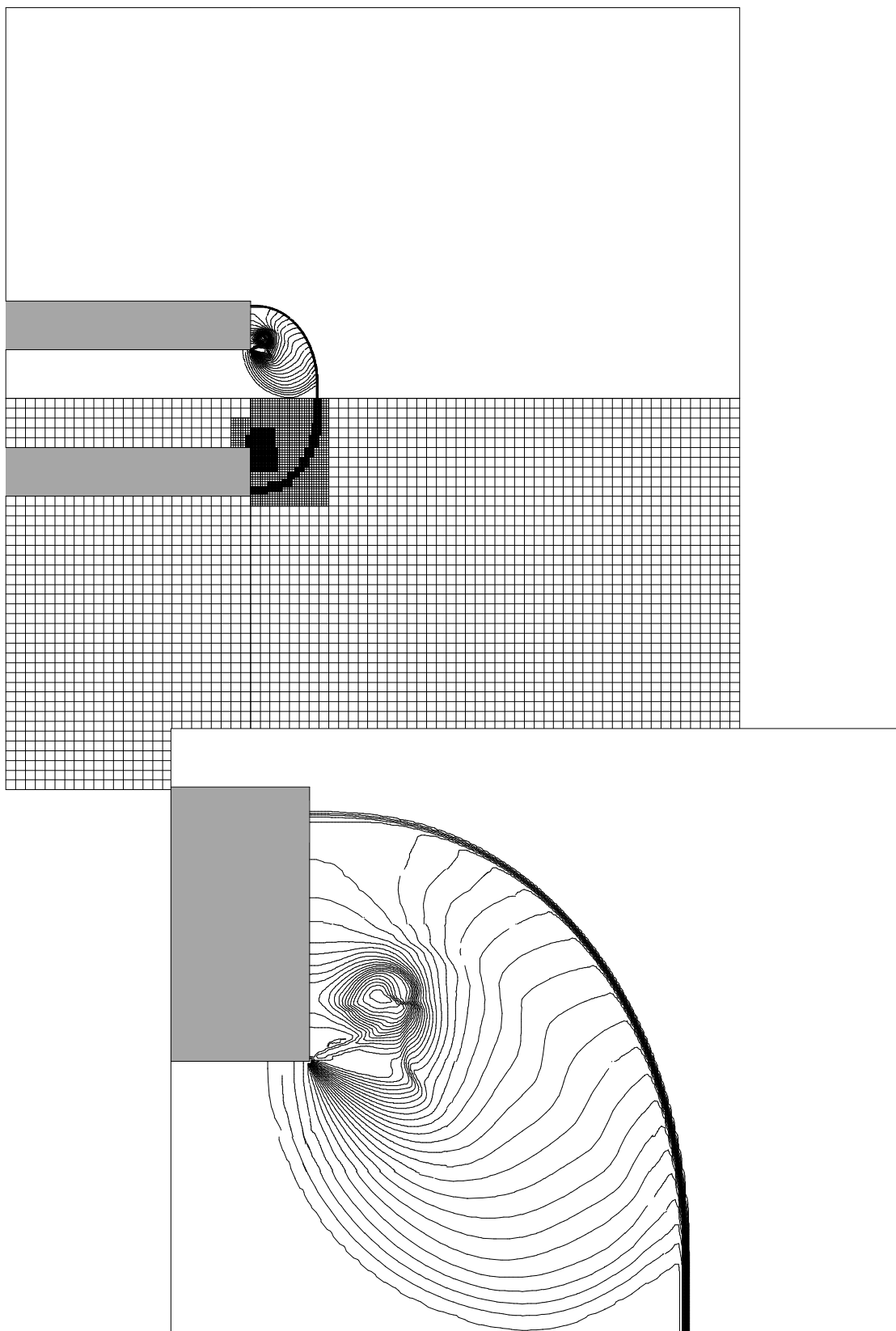


Figure 6.3: The shock diffracts around the exit lip of the tube, cf. figure 6.7.

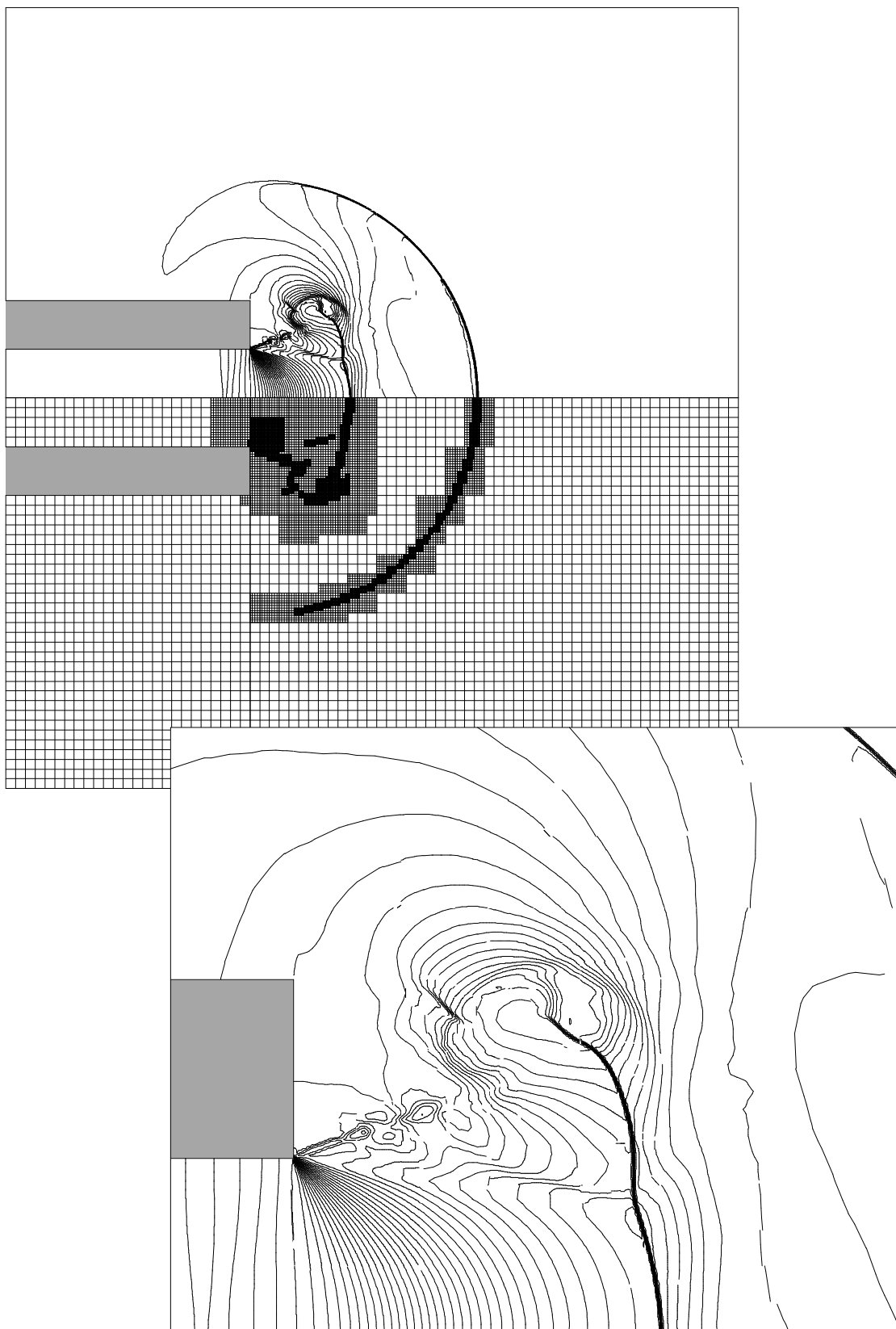


Figure 6.4: An almost spherical blast wave is formed.

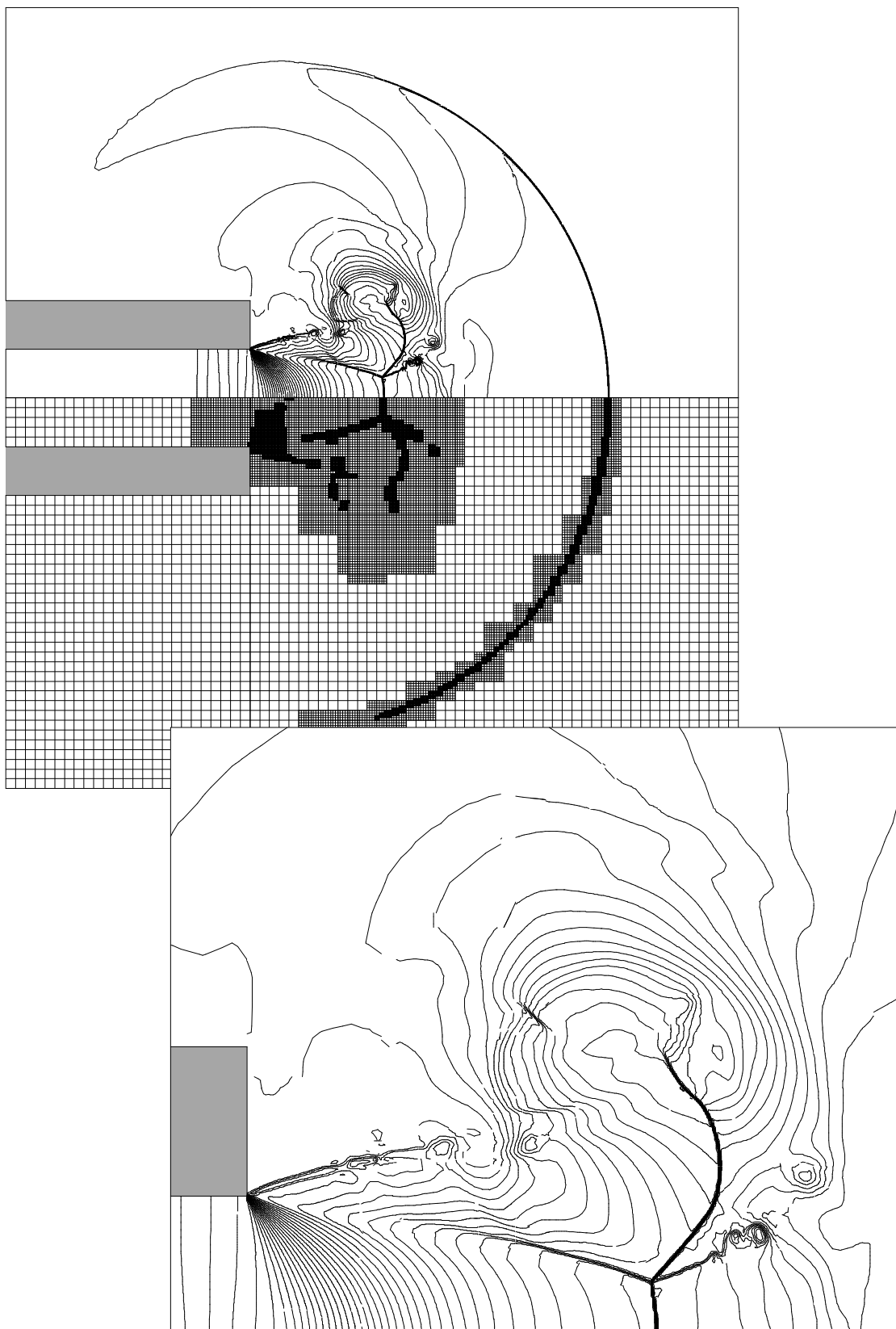


Figure 6.5: The Mach disk and vortex travel downstream.

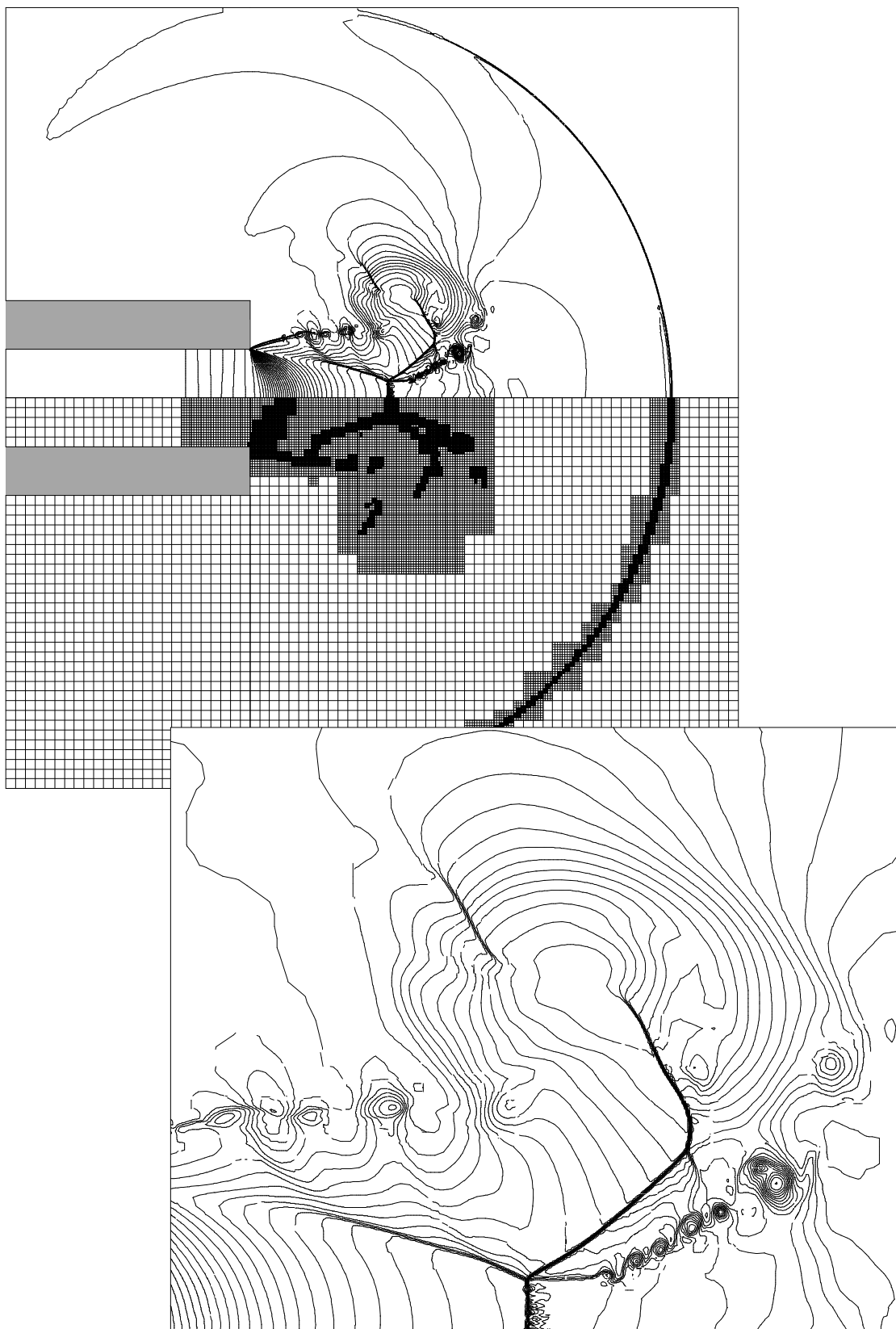


Figure 6.6: The position of the Mach disk has stabilised, cf. figure 6.8.

Figure 6.7: Shadowgraph of the shock diffraction around the exit lip of the tube, taken from Schmidt & Duffy[60].

Figure 6.8: Shadowgraph of the Mach disk and vortex core, note the flow direction is reversed, taken from Schmidt & Duffy[60].